Subsurface Near-Field Microwave Holography

Konstantin P. Gaikovich, Petr K. Gaikovich, Yelena S. Maksimovitch, *Senior Member, IEEE*, and Vitaly A. Badeev

***Abstract*—A new method of near-field electromagnetic holography of subsurface dielectric targets is developed and studied in experiments with the multifrequency microwave system. It is based on the solution of the near-field inverse scattering problem obtained by data of multifrequency measurements of the two-dimensional (2-D) scattered field distribution with the source–receiver system that is located above the surface of a medium with buried dielectric targets. The solution, obtained initially in the lateral k-space representation, can be used to derive tomograms of distributed inhomogeneities or to determine the geometric shape of solid targets with sharp boundaries for further visualization as holography images with a subwavelength resolution. Such a holography method is studied in detail, including the formation of scattered field and signal for various samples in various media, achievable resolution, and effects of multiple scattering.**

***Index Terms*—Holography, inverse problems, microwave imaging, nondestructive testing, reconstruction algorithms, tomography.**

I. Introduction

THE HOLOGRAPHY, as a method of recording and reproduction of the wave reflected from an object, has been proposed by Gabor [1] and applied originally in electron microscopy; then, it has been realized in optics using discovered possibilities of lasers [2], [3]. The classical holography, which has appeared as an analog method of imaging, now involves numerical methods of analysis. Possibilities of using the digital signal processing in the whole process chain of synthetically prepared holographic light wavefronts suitable for observation have been realized in "computer-generated holography" [4], [5]. Then, digital holography has been developed further to deliver three-dimensional (3-D) surface of targets [6], [7]. There are various techniques that are applied in practice, depending on the intended purpose. Similar approaches have been developed to work out various methods of radio holography [8] that has been further applied in radio imaging, radar target identification, remote sensing, and antenna metrology.

Recently, results related to possible applications of radio holography for sounding of subsurface objects and for defectoscopy have been published [9]. Unlike this work, where visualization possibilities of strongly scattering metal targets have been considered, in this paper, we propose here to retrieve the shape of weakly scattering low-contrast dielectric objects. For that, we develop further a method of multifrequency near-field scanning tomography that was proposed and realized in the microwave tomography (visualization of retrieved 3-D distribution of complex permittivity) in [10] and [11] and holography (visualization of the numerical target shape) of subsurface dielectric inhomogeneities [12].

Tomography problems always include the statement of corresponding 3-D inverse problems that is typically based on the solution of 3-D integral equations of the first kind. It leads to strong limitations of the grid size used in calculations and, hence, to limitations of the achievable resolution. In some of early proposed methods of subsurface tomography (radiometry, impedance, low-frequency sounding of earth crust [10], total-internal-reflection tomography [13], [14]), problems have been reduced to one-dimensional (1-D) integral equations by 2-D Fourier transform over transversal coordinates.

We developed this approach for the scanning near-field tomography of inhomogeneities in arbitrary multilayer media using the proposed method of data acquisition [11]. It involves in analysis 2-D lateral distribution of the scattered field measured by scanning at the unchanging source–receiver relative position in dependence on a third parameter that provides the depth sensitivity (such as signal frequency, sensor elevation, or its size). This scheme enables one to make 2-D Fourier transform of the integral equation in the Born approximation and reduce this problem to the multiple solution of 1-D integral equation; also, an iterative algorithm has been proposed to obtain some corrections beyond this approximation. Necessary Green functions have been obtained explicitly in [11] using the plane wave decomposition of fields. A multifrequency and a multilevel scheme of measurements have been suggested and, to retrieve 3-D complex-valued permittivity distributions from the solution of Fredholm integral equations of the first kind, algorithms based on the generalized discrepancy principle in the complex Hilbert space W_2^1 have been worked out and studied in the numerical simulation in applications to multifrequency microwave tomography and to multilevel perfect lens tomography. It was shown [11] that there is the possibility to realize a subwavelength resolution in tomography of subsurface targets in the near-field zone using the property

Manuscript received November 28, 2014; accepted May 24, 2015. This work was supported in part by the Russian Foundation for Basic Research under Grant 12-02-90028_Bel, Grant 13-07-97028_r, and Grant 13-02-12155_ofi_m, in part by the Belarusian Republican Foundation for Fundamental Research under Grant T12R-133, and in part by the Ministry of Education and Science of Russian Federation under agreement on August 27, 2013 Grant 02.B.49.21.0003 between Ministry of Education and Science and Lobachevsky State University of Nizhny Novgorod and within frameworks of the state plan in the region of scientific activity (the project part code no. 1727).

K. P. Gaikovich is with the Institute for Physics of Microstructures RAS, GSP 105 Nizhny Novgorod, Russia, and also with the Lobachevsky State University of Nizhny Novgorod, Nizhny Novgorod 603950, Russia (e-mail: gaikovich@mail.ru).

P. K. Gaikovich is with the Institute for Physics of Microstructures RAS, GSP 105 Nizhny Novgorod, Russia (e-mail: gaikovich@ipmras.ru).

Y. S. Maksimovitch and V. A. Badeev are with the Institute of Applied Physics NAS of Belarus, Minsk 220072, Belarus (e-mail: makhel@iaph.basnet.by; vitan_bad@rambler.ru).

Color versions of one or more of the figures in this paper are available online at http://ieeexplore.ieee.org.

Digital Object Identifier 10.1109/JSTARS.2015.2443035

of small-aperture antennas to generate and receive evanescent waves. This approach is the only way when it is impossible to use higher frequencies (or short pulses)—technically, or because of a high extinction in media.

Such a multifrequency near-field scanning tomography has been realized experimentally with the microwave system [12], where we hit a problem that consisted of a high noise level related to the scattering by surface inhomogeneities (so high that it was difficult to discern the signal scattered from subsurface targets placed under a visually smooth surface at separated frequencies). This problem has been surmounted using the transformation of the multifrequency inverse scattering problem to that in the time domain for a synthesized pseudopulse, and good results of such a tomography have been demonstrated. Also, for targets with a homogeneous inner structure, a method to obtain holography images of their shape has been proposed, and first results have been obtained.

Here, we develop and study this method in its application to various subsurface targets in various media based on experiments with the same setup as in [12]. Calculated field distributions and kernels of integral equations are compared to those obtained from experiments; the holography method is generalized for nonsimply connected targets to determine also the shape of intrusions or hollows. The effect of the secondary scattering on results obtained in Born approximation is demonstrated and discussed.

II. Inverse Scattering Problem. Subsurface Tomography and Holography

Let us consider a scattering region with the complex permittivity $\varepsilon(\mathbf{r}) = \varepsilon_0 + \varepsilon_1(\mathbf{r})$ that is embedded in a half-space $z \le 0$ with $\varepsilon = \varepsilon_0$ (see Fig. 1).

The total field at the frequency ω is a sum of probing and scattered field components $\mathbf{E}(x, y, \omega) = \mathbf{E}_0(x, y, \omega) + \mathbf{E_1}(x, y, \omega)$. For the scheme of measurements with the fixed source–receiver vector $\boldsymbol{\delta}\mathbf{r}$, when the structure of the probing field is invariable relative to the receiver position, it is possible to express the k-space spectrum (2-D inverse Fourier transform over x and y) of the scattered field in frameworks of the Born approximation

$$\begin{aligned} &E_{1i}(\omega, k_x, k_y, z, \boldsymbol{\delta}\mathbf{r}) \\ &= -4\pi^3 i\omega \int_{z'} \varepsilon_1(k_x, k_y, z') \left[\int_{-\infty}^{\infty} \int_{-\infty}^{\infty} \mathrm{e}^{-i\kappa_x \delta x - i\kappa_y \delta y} \right. \\ &\quad \left. \times \int_{z''} [j_i(\omega, \kappa_x, \kappa_y, z'' - z - \delta z) G_{ij}^{12}(\omega, \kappa_x, \kappa_y, z'', z') \right] \\ &\quad \times G_{ji}^{21}(\omega, \kappa_x + k_x, \kappa_y + k_y, z', z) d\kappa_x d\kappa_y dz'' dz' \end{aligned} \tag{1}$$

where G_{ji}^{lk} are k-space components of Green tensors; j_i is the k-space source current distribution (for brevity, we use same notations for k-space representations). As it is possible to see from (1), this equation can be used to solve the inverse scattering problem in various statements. If we consider (1) as a Fredholm integral equation of the first kind, it is possible to use the frequency dependence of the kernel (multifrequency method) or the dependence of the kernel on the height of the point where the scattered field is measured (multilevel method). Without doubt, the multifrequency method is most simple in applications, and this method is studied in further analysis.

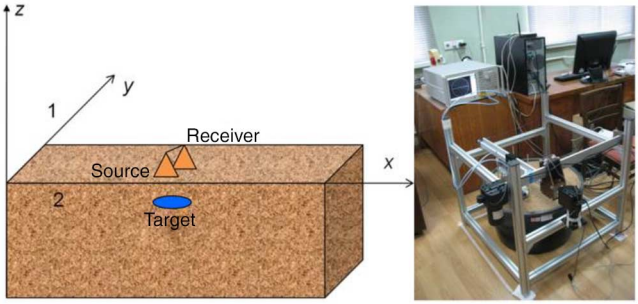

Fig. 1. Scheme of scanning measurements and experimental setup.

A. Tomography

Variations in complex amplitudes of the received signal s are expressed by convolution of the instrument function $\mathbf{F}$ of the receiver and the scattered field $\mathbf{E_1}$

$$s(\mathbf{r}_r) = \int \mathbf{E}_1(\mathbf{r}') \mathbf{F}(x_r - x', y_r - y', z_r, z') dx' dy' dz' \tag{2}$$

where $\mathbf{r}_r$ is the vector determining the receiver position. It leads to the convolution-type equation for our problem

$$s(\mathbf{r}_r, \omega) = \int \varepsilon_1(\mathbf{r}') K(x_r - x', y_r - y', z_r, z', \omega) dx' dy' dz'. \tag{3}$$

From (1) to (3), the transversal spectrum of signal variations measured at fixed z_r is obtained as

$$s(k_x, k_y, \omega) = \int_{z'} \varepsilon_1(k_x, k_y, z') K(k_x, k_y, z', \omega) dz \tag{4}$$

$$\begin{aligned} K(k_x, k_y, z', \omega) &= -4\pi^3 i\omega \int_z \left\{ F_i(k_x, k_y, z, \omega) \right. \\ &\quad \times \int_{-\infty}^{\infty} \int_{-\infty}^{\infty} \mathrm{e}^{-i\kappa_x \delta x - i\kappa_y \delta y} \int_{z''} [j_i(\kappa_x, \kappa_y, z'' - z - \delta z, \omega) \\ &\quad \times G_{ij}^{12}(\kappa_x, \kappa_y, z'', z'', \omega)] \\ &\quad \left. \times G_{ji}^{21}(\kappa_x + k_x, \kappa_y + k_y, z', z, \omega) d\kappa_x d\kappa_y dz'' \right\} dz. \end{aligned}$$

This equation has been used in our algorithm of microwave subsurface tomography that was developed and studied in numerical simulation [11]; however, in our first attempts of its application, it appeared difficult to discern sounded subsurface objects on the measured image of $s(x, y, \omega)$ against the noise produced by the surface scattering. Nevertheless, we have found that it is possible to obtain much better images of

subsurface targets, using the transformation of multifrequency data in the frequency band $\Delta\omega$ to the synthesized pseudopulse

$$s(x_r,y_r,t)=\int_{\Delta\omega} s(x_r,y_r,\omega)\exp(i\omega t)d\omega = \int \varepsilon_1(\mathbf{r}')K(x_r-x',y_r-y',z_r,z',t)dx'dy'dz' \tag{5}$$

that can be represented in dependence on the effective depth parameter z_s as $s(x_r,y_r,z_s)=s(x_r,y_r,\ t=-2z_s\mathrm{Re}\sqrt{\varepsilon_0}/c)$ (taking into account the light velocity in a medium and the signal path to and from a scattering element)

$$s(x_r,y_r,z_s)=\int \varepsilon_1(\mathbf{r}')K(x_r-x',y_r-y',z_r,z',z_s)dx'dy'dz'. \tag{6}$$

Subsurface inhomogeneities were clearly seen in visualized 2-D images of $|s(x_r,y_r,z_s)|$. The strong maximum of $|s(z_s)|$observed in every point of the scanning region (x_r,y_r) marks the value of z_s that corresponds to the surface scattering responsible for the bad quality of data at separate frequencies. The success of this analysis was our motivation to make the same transformation in (4)

$$s(k_x,k_y,t)=\int_{\Delta\omega} s(k_x,k_y,\omega)\exp(i\omega t)d\omega \tag{7}$$

where $s(k_x,k_y,z_s)=s(k_x,k_y,\ t=-2z_s\mathrm{Re}\sqrt{\varepsilon_0}/c)$. It leads to the new equation that relates the complex permittivity spectrum to the complex-valued synthesized pseudopulse of the signal lateral spectrum

$$\begin{aligned} s(k_x,k_y,z_s) &= \int_{z'} \varepsilon_1(k_x,k_y,z')K(k_x,k_y,z',z_s)dz' \\ K(k_x,k_y,z',z_s) &= \int_0^\infty K(k_x,k_y,z',\omega) \\ &\quad \exp(-i\omega 2z_s\mathrm{Re}\sqrt{\varepsilon_0}/c)d\omega. \end{aligned} \tag{8}$$

To simplify notation in (8) and below, we use the same symbols for values and their Fourier transforms, so they are determined by their arguments.

The solution of the Fredholm integral equation (8) is obtained with the algorithm based on the generalized discrepancy principle in the complex Hilbert space W_2^1 [11]. In frameworks of this method, to obtain the solution of (8), the generalized discrepancy should be minimized up to the level of the error parameter $\delta s^2(k_x,k_y)=\sup\|\delta s\|^2_{L_2}=\sup\int_{\Delta z_s}|\mathbf{K}\varepsilon_1-s(k_x,k_y,z_s)|^2dz_s$ in k-space. In practice, it is difficult to obtain the proper estimation of this noise parameter for each pair (k_x,k_y), and it is suitable to use the universal averaged (over the k-range of analysis) value $<\delta s^2>=\frac{1}{\Delta k_x\Delta k_y}\int_{\Delta z_s}\iint \delta s^2(k_x,k_y,z_s)dk_xdk_ydz_s$ calculated by pseudopulse variations $\delta s(x,y,z_s)$ obtained by the data of measurements in the same range of analysis, but without buried targets. Taking into account the corresponding expression for the signal norm $<s^2>=\int_{\Delta z_s}\iint s^2(k_x,k_y,z_s)dk_xdk_ydz$, it is possible to introduce the signal-to-noise ratio (SNR) as $SNR=\sqrt{<s^2>/<\delta_S^2>}$.

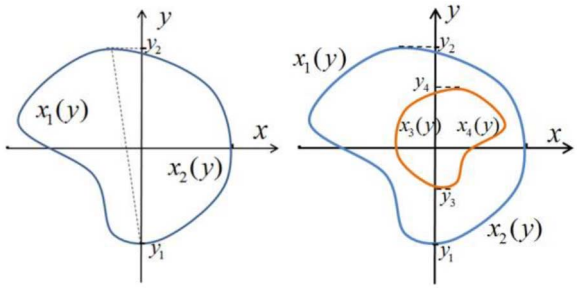

Fig. 2. *Left*: a target shape in z-section as two functions $x_1(y,z)$, $x_2(y,z)$. *Right*: shape of the target with a hole that is defined by functions $x_3(y,z)$, $x_4(y,z)$.

It should be mentioned that for such equations, typically, the dependence of retrieval accuracy on this parameter is not sharp.

From the solution of (8) in k-space, the desired 3-D structure of complex permittivity is obtained by 2-D inverse Fourier transform

$$\varepsilon_1(x,y,z)=\iint \varepsilon_1(k_x,k_y,z)\exp(ik_xx+ik_yy)dk_xdk_y. \tag{9}$$

B. Holography

In practice, subsurface targets mostly have a homogeneous internal structure. If it is known *a priori* that the permittivity of a target $\varepsilon_1=\varepsilon_1^0=const$, then the holography problem, i.e., the problem of target shape retrieval, can be solved using k-space solution $\varepsilon_1(\kappa_x,\kappa_y,z)$ of (8). For that, we express the shape of the target as two functions $x_1(y,z)$ and $x_2(y,z)$ shown in Fig. 2 (left) in a z-section.

Assuming that $x_1(y,z)$, $x_2(y,z)$ are single-valued functions, the retrieved k-space permittivity spectrum can be written as the Fourier transform with finite limits

$$\begin{aligned} \varepsilon_1(k_x,k_y,z) &= \frac{1}{4\pi^2}\int_{y_1}^{y_2}\int_{x_1(y)}^{x_2(y)} \varepsilon_1^0 e^{-ik_xx-ik_yy}dxdy \\ &= \frac{\varepsilon_1^0}{4\pi^2}\int_{y_1}^{y_2}\exp(-ik_yy)\frac{1}{ik_x}(e^{-ik_xx_1(y)}-e^{-ik_xx_2(y)})dy. \end{aligned} \tag{10}$$

Then, making the inverse Fourier transform of (10) over k_y, we obtain the complex-value transcendent equation

$$\varepsilon_1(k_x,y,z)=\frac{\varepsilon_1^0}{2\pi ik_x}(e^{-ik_xx_1(y,z)}-e^{-ik_xx_2(y,z)}) \tag{11}$$

that is equivalent to the system of two real-valued equations. The desired shape of the target expressed by two functions $x_1(y,z)$, $x_2(y,z)$ is obtained from this equation using the solution $\varepsilon_1(\kappa_x,\kappa_y,z)$of (8). It should be mentioned that this equation is overdetermined: it can be solved at each value of k_x that makes possible to optimize the solution. Depending on available conditions, the value of ε_1^0 may be known *a priori*, or obtained from tomography results (9), or from the solution of (11) as an expanded system with some extra equations with some different values of k_x.

In fact, due to the nonlinearity of the problem, the solution algorithm may be trapped into local minima, however, in our numerical simulation as well as in processing of experimental data it did not appear. In solving, we used the method of exhaustive search over the set of possible values of functions x_1 and x_2 with a step small enough to minimize the quadratic discrepancy for each pair of their arguments (y, z). Best results are obtained at values of k_x of the target transversal spectrum close to the value $k_x = 2\pi/L_t$, where L_t is an estimation of the target's transversal size by visualized pseudopulse image. To obtain the clearest image, this method has been repeatedly applied at various values of k_x around this value—such as in optical focusing. It is clear that a similar equation can be written for the shape expressed by functions $y_1(x, z),\ y_2(x, z)$.

It is possible to generalize this holography method for objects with inclusions of another material with permittivity $\varepsilon_1 = \varepsilon_1^{02}$. In this case, it is also necessary to obtain the shape of this hole defined by two functions $x_3(y, z),\ x_4(y, z)$ as it is shown in Fig. 2. Making the same transformations as above, one has the complex-value transcendent equation

$$\varepsilon_1(k_x, y, z) = \frac{\varepsilon_1^0}{2\pi i k_x}(e^{-ik_x x_1(y,z)} - e^{-ik_x x_2(y,z)}) + \frac{(\varepsilon_1^{02} - \varepsilon_1^0)}{2\pi i k_x}(e^{-ik_x x_3(y,z)} - e^{-ik_x x_4(y,z)}). \tag{12}$$

This equation should be solved as a system of two or more equations with different values of k_x. Values of $\varepsilon_1^0, \varepsilon_1^{02}$ can be determined from the results of tomography analysis.

Here, it should be stressed that it is theoretically impossible to obtain the exact positions of target boundaries using tomography images obtained from (9)—even neglecting retrieval errors, because it is well known that step-functions cannot be expressed exactly close to the points of gradient discontinuity even by arbitrary long Fourier series that represent (9) in numerical calculations. In such points, the Dini test for pointwise convergence of Fourier series is not satisfied, and the results are distorted by Gibbs effect. So, if it is known *a priori* that we deal with such a target, the problem is to determine the exact position of its boundaries on smoothed holography images. The proposed method is just a proper rigorous solution of this problem.

III. Multifrequency Tomography and Holography

A. Study of Integral Equations

This theory has been realized in algorithms of multifrequency microwave tomography and holography and studied experimentally. Measurements of signal complex amplitudes for 801 frequencies in the range 1.6–7.0 GHz obtained by 2-D lateral scanning are used in analysis. The source–receiver system based on the vector network analyzer Agilent E5071B includes two identical transmitting and receiving planar bowtie antennas in bistatic configuration placed in y-direction with 3.8 cm length of arms and 5.4 cm width, placed in y-direction; the fixed distance between centers of antennas was $\Delta x = 7.5$ cm. They are scanning together in the rectangle $x - y$ area above the buried targets.

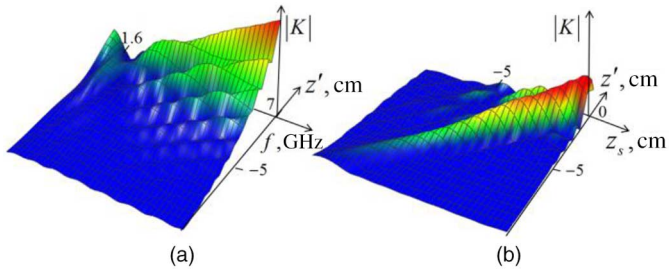

Fig. 3. (a) Amplitude of kernel $|K(X = 0, Y = 0, z', \omega = 2\pi f)|$ of (6). (b) Kernel $|K(X = 0, Y = 0, z', z_s)|$ of (8).

Current distributions on such antennas are quite sharply localized at the center of their surface, so they have a very broad spatial spectrum, where components with $k_x, k_y > 2\pi/\lambda$ dominate, and, according to (1), they form a broad near-field spectrum of the signal. It makes possible to realize the subwavelength resolution of targets in the proposed tomography method that has been demonstrated in [12].

Theoretically, the depth of such subwavelength tomography is not limited—restrictions are related only to the achievable sensitivity. But in practice, at a fixed sensitivity, because of the fading of evanescent components with depth, the accuracy of tomography decreases with the increase in target depth, whereas its resolution tends gradually to Rayleigh limitations. It should also be noted that the accuracy of retrieval depends on the target depth as well as on its shape, so it can be determined only on the base of the case study—from numerical or real experiments.

Taking into account that subsurface inhomogeneities are typically solid targets with sharp boundaries, here we study the method of computer holography for such targets with various permittivities: foam ($\varepsilon_0 = 1$), epoxy ($\varepsilon_0 = 3.4 + 0.03\ i$), concrete ($\varepsilon_0 = 6.0 + 0.05\ i$), and living tissue (pig's fat) ($\varepsilon_0 = 11.3 + 2.2\ i$) buried in sand ($\varepsilon_0 = 4.0 + 0.5\ i$) or dipped in engine oil ($\varepsilon_0 = 2.5 + 0.2\ i$).

To study the formation and spatial resolution of the measured signal $s(x_r, y_r, \omega)$ at separate frequencies and of its synthesized pseudopulse $s(x_r, y_r, z_s)$ at various values of effective depth of scattering z_s, it is necessary to study kernels of corresponding 3-D equations (4) and (6). These kernels are calculated using transformations

$$K(X,Y,z',z_s) = \iint K(k_x, k_y, z', z_s)\exp[ik_x X + ik_y Y]dk_x dk_y \tag{13}$$

$$K(X, Y, z', \omega) = \int K(X, Y, z', tc/2\mathrm{Re}\sqrt{\varepsilon_0})\exp(i\omega t)dt \tag{14}$$

where $X = x_r - x',\ Y = y_r - y'$. Results of their calculation for targets in sand are shown in Fig. 3.

As it can easily be seen, the near-surface contribution of the kernel (4) in the signal is dominated (that makes it difficult to discern the field scattered by targets from the noise introduced by surface inhomogeneities), whereas the kernel of (6) for the synthesized pulse has maxima at various depths throughout the

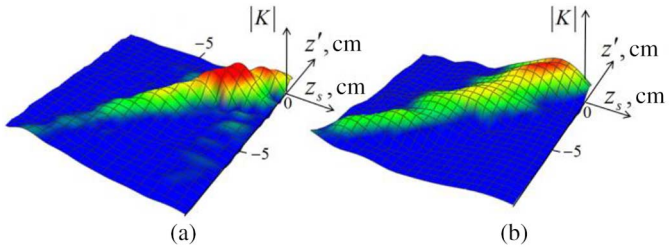

Fig. 4. Experimental kernel $K(X=0, Y=0, z', z_s)$ in (8) for scattering elements at $X=0,\ Y=0$ in (a) sand and (b) oil.

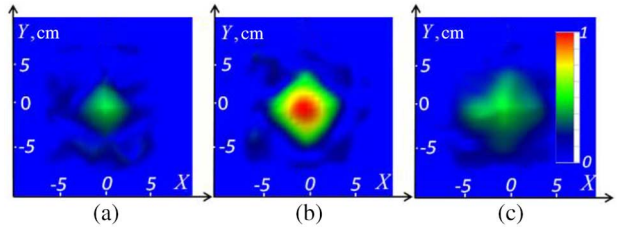

Fig. 5. Transversal structure of experimental kernel $|K(X, Y, z', z_s - z')|$ in (8). (a) $z' = -1$ cm. (b) $z' = -3$ cm. (c) $z' = -7$ cm.

interval of sounding. Such a kernel provides much better conditions for the equation solving—it is much closer to the perfect kernel expressed by a line of δ-functions.

Of course, it is interesting to compare the theoretical kernel in (6) with that obtained from experiments. There is a quite simple way to determine the kernel K in (8) from measurements of weakly scattering thin test samples with the known shape and permittivity placed at different depths z_0 throughout the sounded area. Corresponding lateral spectra are expressed as $\varepsilon_1(k_x, k_y, z') = \varepsilon_t(k_x, k_y)\delta(z' - z_0)$, and the kernel is obtained as $K_1(k_x, k_y, z_0, z_s) = s(k_x, k_y, z_0, z_s)/\varepsilon_t(k_x, k_y)$. Then, the kernel of integral equation (6) is obtained from (13).

In Fig. 4, it is possible to see such experimental kernels $K(X=0, Y=0, z', z_s)$ in (6) obtained from measurements with thin test samples ($\Delta z = 0.5$ cm) in sand and oil.

One can see a good correspondence between the theoretical [Fig. 3(b)] and experimental [Fig. 4(a)] results for targets in sand. Also, it is possible to see that measurements in oil [Fig. 4(b)] have a better sensitivity to deep targets because it is a less absorbing medium than sand [Fig. 4(a)].

In Fig. 5, the transversal structure of experimental kernel $K(X, Y, z', z_s)$ in (6) obtained from measurements in sand is demonstrated assuming that the effective depth $z_s$of scattering is equal to the depth $z'$of a point scattering element at three values of z'. It can be considered as a point spread function. It can be seen in Fig. 5 that, like in Fig. 4, the signal scattering has its maximum close to $z' = -3$ cm. The width of this function grows with depth; however, it remains sharp enough near its center that provides a good transversal resolution of images.

B. Results for Low-Contrast Targets in Sand

To study the depth resolution of proposed methods of tomography and holography, results for parallelepiped foam samples with sizes $4 \times 4 \times 1$ cm^3 (see insertion in Fig. 6) have been obtained. Their lateral sizes correspond

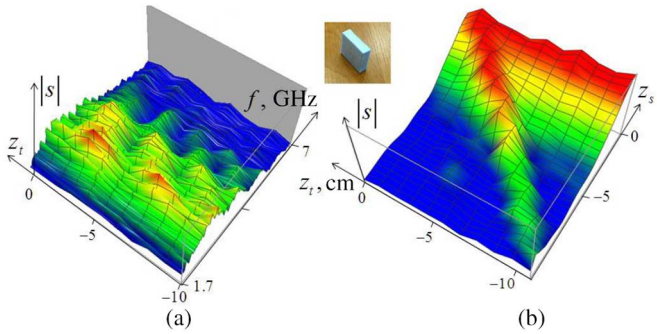

Fig. 6. (a) Signal frequency spectrum of targets at depths $z_t = -1, -2, \ldots, -10$ cm measured in the center point ($x = 10$ cm, $y = 10$ cm) above targets in sand. (b) Corresponding pseudopulse amplitude versus effective depth of target z_s.

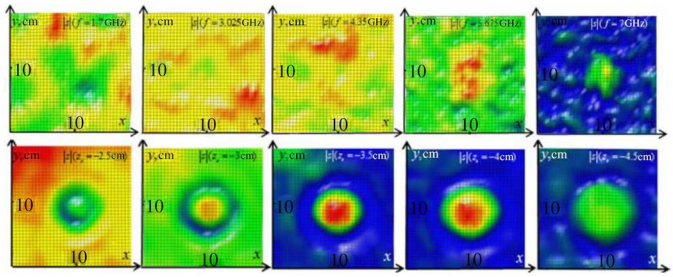

Fig. 7. Top: images of signal amplitude $|s(x, y, \omega = 2\pi f)|$ for target at $z_t = -3$ cm at five frequencies in sand. Lower row: pseudopulse amplitude $|s(x, y, z_s)|$ images for target at $z_t = -3$ cm at five values of effective depths z_s.

to the shortest free-space wavelength $\lambda_{\min} = 4$ cm in analysis. In Fig. 6(a), the frequency dependence of the signal amplitude measured above the target center position $|s(x = 10\text{ cm}, y = 10\text{ cm},\ 2\pi f)|$ for targets at depths $z_t = -1, -2, \ldots, -10$ cm is demonstrated. The corresponding dependence of the pseudopulse amplitude $|s(x = 10\text{ cm}, y = 10\text{ cm},\ z_s)|$on the effective depth z_s is shown in Fig. 6(b).

As it is seen in Fig. 6(a), the frequency band of analysis covers the main part of the scattering spectrum. For centimeter-size inhomogeneities, the signal falls drastically with decrease in scattering at lower frequencies; at higher frequencies, the signal falls because of the increase in absorption. Unfortunately, it is impossible to discern targets in multifrequency data. But in pseudopulse data in Fig. 6(b), targets are clearly seen. That demonstrates the possibility to realize a good depth resolution, so that one can estimate their depth position. It is very important to obtain a good solution of inverse problem (8). In the near-surface region, one can see the strong maximum in the pseudopulse amplitude related to the surface-antenna multiple scattering.

In Fig. 7, the comparison of signal amplitude images at separate frequencies ($f = 1.7, 3.025, 4.35, 5.675, 7$ GHz) with images of pseudopulse amplitude at various values of the effective depth ($z_s = -2.5; -3; -3.5; -4; -4.5$ cm) is given. Again, one can see that it is very difficult to discern targets in signal images measured at separate frequencies in the band of analysis (upper row in Fig. 7).

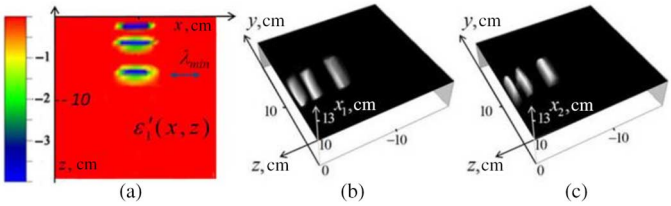

Fig. 8. (a) Results of subsurface tomography of targets at depths $z_t = -1, -3,$ and -7 cm (vertical section at $y = 10$ cm) in sand. (b) and (c) Holography images of these targets expressed by functions $x_1(y,z), x_2(y,z)$. Arrow marks the minimal wavelength in analysis.

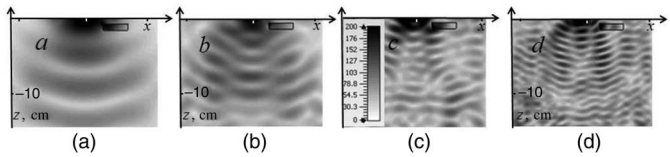

Fig. 9. Distribution of total field $|E(x,z)|$ in vertical section $y = 10$ cm at frequencies: (a) f $= 1.6$ GHz; (b) 3 GHz; (c) 5 GHz; and (d) 7 GHz.

In pseudopulse data (lower row), the noise related to surface-target scattering is much suppressed, and targets are clearly seen in some range of effective depth z_s. So, one can discern subsurface objects in pseudopulse images and estimate their maximal transversal sizes. It is also worth mentioning that the clearest image is seen at $z_s \approx z_t$, so one can easily estimate the depth localization of target.

In Fig. 8, results of tomography and holography for this target at three different depths $z_t = -1, -3,$ and -7 cm are shown. Tomography results are obtained from the solution of (8); holography images—from (11), assuming signal-to-noise level SNS $= 7,$ 20, and 5, respectively. Pseudopulse data in the region $-0.5 \le z_s \le -10$ cm have been used in analysis. Results demonstrate a subwavelength resolution of images and good accuracy (not less than 20%) in determination of dielectric parameters, shape, and position of buried targets. At deeper depths, outside the near zone for the longest wavelength, images of targets gradually become fuzzy.

To study the applicability of Born approximation, field distributions have been calculated for the foam sample at the depth $z_t = -1$ cm at four frequencies (see Fig. 9).

Distributions of the probing field in Fig. 9 are practically unperturbed by the foam sample, so (8) is suitable for analysis. At lower frequencies, the target appears inside the near-field zone, whereas at higher frequencies, it is in the range where the wave (propagating) components of the probing field dominate.

In Fig. 10, results of holography analysis for epoxy sphere (billiard ball) are presented as an example of the target with an extremely low dielectric sample-medium contrast ($\varepsilon_1^0 \approx 0.5$).

The SNR for a such low-contrast target is less than that for targets shown in Figs. 7 and 8 (the value SNS $= 4$ was assumed in analysis). However, the Born approximation is fulfilled much better in this case. As a result, holography images of the target are retrieved with a good quality.

C. Results for Targets in Oil

Measurements in a liquid medium have obvious advantages: perfect plane surface, absence of volume inhomogeneities,

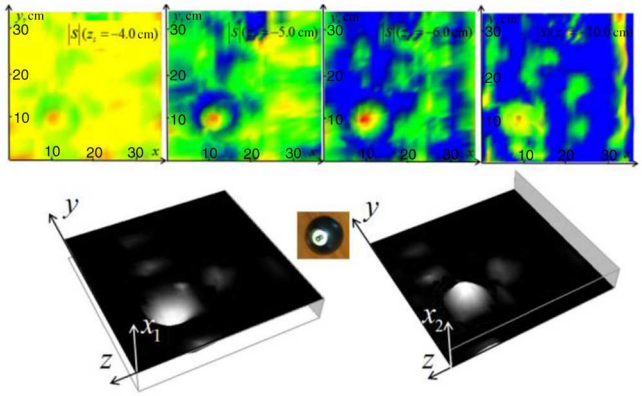

Fig. 10. Upper row: images of signal amplitude $|s(x,y,z_s)|$ for epoxy sample at $z_t = -5$ cm at $z_s = -4, -5, -6, -10$ cm in sand. Lower row: holography images of target expressed by functions $x_1(y,z), x_2(y,z)$. Insertion: target.

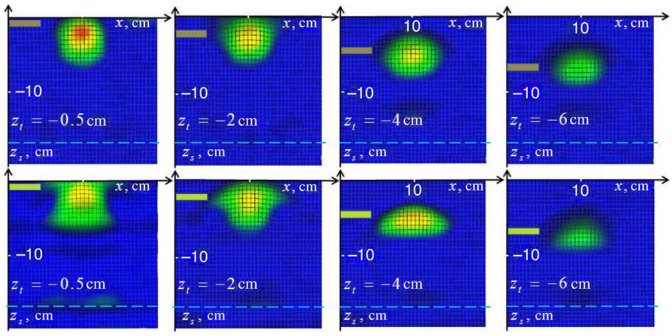

Fig. 11. Images of pseudopulse amplitude $|s(x,\ z_s)|$ at $y = 10$ cm for concrete (upper row) and fat (lower row) targets with sizes $4 \times 4 \times 1$ cm^3 at target depths $z_t = -0.5,\ -2,\ -4,$ and -6 cm in oil. Rectangle insertions determine target positions. Dashed line marks the bottom level of the tank.

easier positioning of targets, and, as a result, a low level of related noise and errors, so that value SNR $= 30$ was assumed in analysis. In this study, we used targets from concrete as a material with a relatively small dielectric contrast, and fat as a material with large real and imaginary parts of permittivity.

At first, to compare results to those obtained in sand, experiments have been carried out for samples with the same sizes $4 \times 4 \times 1$ cm^3. The specific character of scattering from these targets is seen in dependence $|s(x,\ z_s)|$ of the signal on the effective depth of scattering z_s shown in section along the line x passed above the centers of targets (Fig. 11).

As it can be seen from images for targets at depths $z_t = -0.5; -2$ cm, fat images are wider and deeper as compared to concrete images. We think that it may be explained by secondary surface-target scattering because of the large fat permittivity. In contrast to shallow-buried targets, for targets at depths $z_t = -4; -6$ cm, fat targets look thinner, which we consider as an effect of larger absorption in the fat material.

In Fig. 12, distributions of total and scattered field for these samples at depth $z_t = -1$ cm are shown.

As it is possible to see, the field scattered from the fat sample is somewhat greater than that from the concrete sample that has lower permittivity. Distortions of the field inside the fat sample at high frequencies produce secondary scattering. The field distribution for the concrete sample is very similar to that for

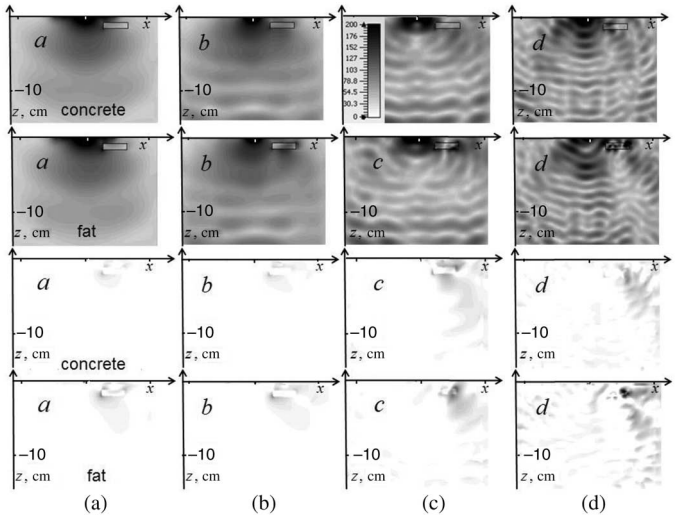

Fig. 12. Upper two rows: a vertical section of total field $|E(x,z)|$ for concrete and fat samples at frequencies: (a) $f = 1.6$ GHz; (b) 3 GHz; (c) 5 GHz; and (d) 7 GHz in oil. Lower two rows: scattered field $|E_1(x,z)|$ for these samples.

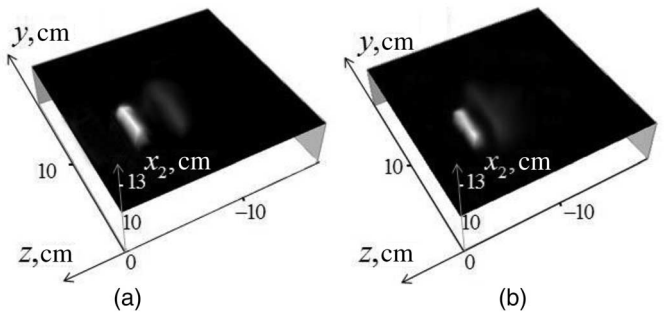

Fig. 13. Results of subsurface holography of targets at depth $z_t = -4$ cm in oil expressed by functions $x_2(y,z)$. (a) Concrete target. (b) Fat target.

the foam sample shown in Fig. 9, where the field distribution is practically unperturbed by the target.

In Fig. 13, holography images for concrete and fat targets at depth $z_t = -5$ cm are demonstrated for parts of their shape represented by function x_2 (see Fig. 2).

Results demonstrate good shape retrieval for both targets. Also, small artifacts are seen.

More serious problems have been encountered in experiments with thicker samples and samples with a hollow. In Fig. 14(a), the dependence of the pseudopulse amplitude above the target center position $|s(x = 10\text{ cm}, y = 10\text{ cm}, z_s)|$ for the concrete sample with sizes $4 \times 4 \times 3$ cm^3 at depths $z_t = -0.5, -1, \ldots, -10$ cm is shown; in Fig. 14(b), one can see results for the concrete sample with the same sizes but with the foam intrusion $2 \times 2 \times 1$ cm^3 inside it.

Results demonstrate that thick samples in Fig. 14 are seen in a wider range of effective scattering depth parameter z_s than thin samples in Fig. 6(b). One can see that the pseudopulse distribution for the target with intrusion in Fig. 14(b) is sensitive to this hollow and has two maxima—as opposed to that without a hollow in Fig. 14(a).

In Fig. 15, dependences of the signal amplitude $|s(x,\ z_s)|$ on the effective scattering depth parameter z_s along the line x passed above targets' centers are shown.

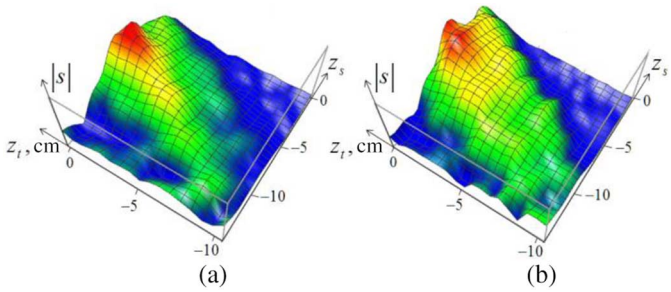

Fig. 14. Images of pseudopulse amplitude $|s(x = 10\text{ cm}, y = 10\text{ cm},\ z_s)|$ at target depths $z_t = -0.5, -1, 1.5, \ldots, -10$ cm: (a) for concrete target with sizes $4 \times 4 \times 3$ cm^3; (b) for concrete target with sizes $4 \times 4 \times 3$ cm^3 with hollow $2 \times 2 \times 1$ cm^3.

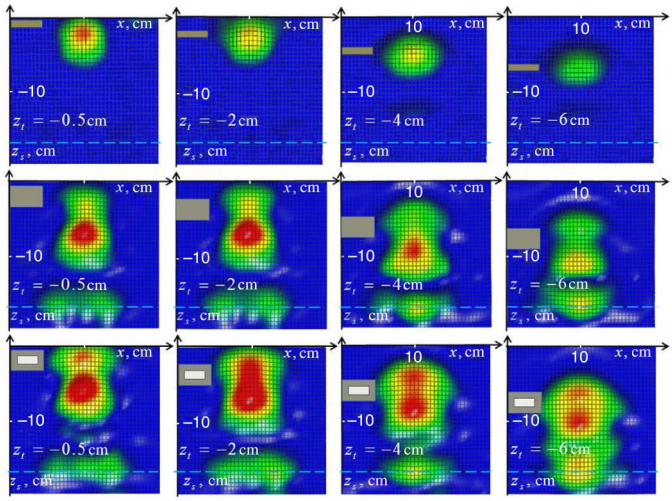

Fig. 15. Upper row: images of pseudopulse amplitude $|\mathrm{s}(x,\ \mathrm{z_s})|$ at $y = 10$ cm for concrete sample with sizes $4 \times 4 \times 1$ cm^3. Middle row: images for concrete sample with sizes $4 \times 4 \times 3$ cm^3. Lower row: images for concrete target with sizes $4 \times 4 \times 3$ cm^3 with a hollow $2 \times 2 \times 1$ cm^3. Depths of targets: $z_t = -0.5, -2, -4,$ and -6 cm. Rectangle insertions indicate depth positions of targets. Dashed line marks the bottom level of the tank.

One can see that the distributions for thick samples differ considerable from those for the thin sample shown in the upper row. These images are spread in much wider range over z_s as compared to results for the thin sample.

In Fig. 16, results of holography analysis are demonstrated for these three targets placed at the depth $z_t = -5$ cm. At that, for the target with a foam intrusion shown in Fig. 16(c), results are obtained from solution of (12). In Fig. 16(c), the image of the outer shape of sample represented by the function x_1 is combined with the image of the hollow shape represented by the function $x_3(y,z)$ (introduced in Fig. 2). One can see in Fig. 16(a) that the image of the thin target is retrieved without strong distortions. The image of the thick target without hollow in Fig. 16(b) is seen between two artifacts, but the true image represents the shape of the sample quite correctly.

Especially impressive results are presented in Fig. 16(c) for the sample with the foam intrusion that demonstrates the shape retrieval of both outer and inner boundaries of this nonsimply connected object. It is also interesting to mention a stochastization of artifacts' structure for this sample. Probably, these artifacts can be explained by the interference at the multiple scattering between the receiving antenna and samples with

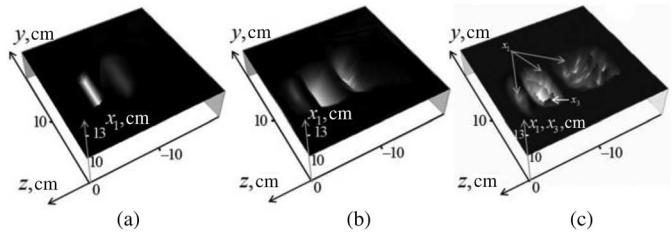

Fig. 16. Results of subsurface tomography of targets at depth $z_t = -5$ cm in oil. (a) Image of concrete target with sizes $4 \times 4 \times 1$ cm^3 represented by function $\mathrm{x}_1(y, z)$. (b) Image of concrete target $4 \times 4 \times 3$ cm^3 represented by function $x_1(y, z)$. (c) Image of concrete target $4 \times 4 \times 3$ cm^3 [function $x_1(y, z)$] with foam intrusion $2 \times 2 \times 1$ cm^3 [function $x_3(y, z)$].

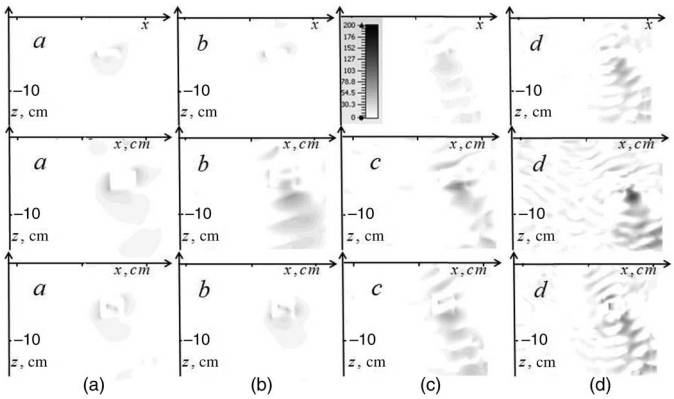

Fig. 17. Scattered field $|E_1(x, z)|$ for three samples at: (a) $f = 1.6$ GHz; (b) 3 GHz; (c) 5 GHz; and (d) 7 GHz. Upper row: for concrete target $4 \times 4 \times 1$ cm^3; middle row: for concrete target $4 \times 4 \times 3$ cm^3; and lower row: for concrete target $4 \times 4 \times 3$ cm^3 with hollow $2 \times 2 \times 1$ cm^3.

the contribution of the probing field reflected by the receiving antenna. The possibility of such sample-antenna scattering demonstrates the similar effect of the target-bottom scattering seen in Fig. 15 near the tank bottom level (dashed line). Nevertheless, in spite of this obstacle, true images in Fig. 16 are observed separately from artifacts and they are free from strong distortions. We hope that this effect can be suppressed to some extent by a proper modification of antenna system.

In Fig. 17, distributions of the scattered field for three concrete above-considered targets are shown at $z_{\mathrm{t}} = -4$ cm.

As it is seen in Fig. 17, the scattered field increases for larger targets, but it is yet small as compared to the probing field, so it is reasonable to apply in analysis the integral equation (8) obtained in Born approximation.

Now, we try to generalize solution algorithms beyond the Born approximation developing a new approach to nonlinear inverse scattering problems based on the dual regularization method in the optimization theory [16].

IV. Conclusion

Results of this paper demonstrate that the proposed method of subsurface holography of dielectric targets in the near zone is effective enough, providing a subwavelength resolution for targets of typical natural materials in various media. We hope that the developed approach can be used in various applications of electromagnetic or acoustic diagnostics, including biomedical diagnostics of tumors, nondestructive testing in defectoscopy, civil engineering, and underground remote sensing.

References

[1] D. Gabor, "A new microscopic principle," *Nature*, vol. 161, no. 4098, pp. 777–778, May 1948.
[2] Yu. N. Denisyuk, "On the reflection of optical properties of an object in a wave field of light scattered by it," *Doklady Akademii Nauk SSSR*, vol. 144, no. 6, pp. 1275–1278, Jun. 1962.
[3] E. N. Leith and J. Upatnieks, "Reconstructed wavefronts and communication theory," *J. Opt. Soc. Amer.*, vol. 52, no. 10, pp. 1123–1130, Oct. 1962.
[4] J. P. Waters, "Holographic image synthesis utilizing theoretical methods," *Appl. Phys. Lett.*, vol. 9, no. 11, pp. 405–407, Oct. 1966.
[5] G. L. Rogers, "Gabor diffraction microscopy: The hologram as a generalized zone-plate," *Nature*, vol. 166, no. 4214, p. 237, Aug. 1950.
[6] U. Schnars and W. Jüptner, *Digital Holography*. New York, NY, USA: Springer, 2005.
[7] E. Lam, X. Zhang, H. Vo, T.-C. Poon, and G. Indebetouw, "Gabor three-dimensional microscopy and sectional image reconstruction using optical scanning holography," *Appl. Opt.*, vol. 48, no. 34, pp. H113–H119, Dec. 2009.
[8] A. P. Anderson, "Microwave holography," *Proc. IEE*, vol. 124, no. 11R, pp. 946–962, Nov. 1977.
[9] V. V. Razevig, S. I. Ivashov, A. P. Sheyko, I. A. Vasiliev, and A. V. Zhuravlev, "An example of holographic radar using at restoration works of historical building," *PIER Lett.*, vol. 1, no. 34, pp. 173–179, Jan. 2008.
[10] K. P. Gaikovich, "Subsurface near-field scanning tomography," *Phys. Rev. Lett.*, vol. 98, no. 18, p. 183902, May 2007.
[11] K. P. Gaikovich and P. K. Gaikovich, "Inverse problem of near-field scattering in multilayer media," *Inverse Prob.*, vol. 26, no. 12, p. 125013, Dec. 2010.
[12] K. P. Gaikovich, P. K. Gaikovich, Ye. S. Maksimovitch, and V. A. Badeev, "Pseudopulse near-field subsurface tomography," *Phys. Rev. Lett.*, vol. 108, no. 16, p. 163902, Apr. 2012.
[13] P. S. Carney, V. A. Markel, and J. C. Schotland, "Near-field tomography without phase retrieval," *Phys. Rev. Lett.*, vol. 86, no. 26, pp. 5874–5876, Jun. 2001.
[14] P. S. Carney, R. A. Frazin, S. I. Bozhevolnyi, V. S. Volkov, A. Boltasseva, and J. C. Schotland, "A computational lens for the near-field," *Phys. Rev. Lett.*, vol. 92, no. 16, p. 163903, Apr. 2004.
[15] K. P. Gaikovich, *Inverse Problems in Physical Diagnostics*. Commack, NY, USA: Nova, 2004.
[16] P. K. Gaikovich, M. I. Sumin, and K. P. Gaikovich, "One-dimensional inverse scattering problems," in *Proc.13th Int. Conf. Transparent Opt. Netw.*, Stockholm, Sweden, 2011, pp. 1–4.

Konstantin P. Gaikovich graduated from the Lobachevsky State University of Nizhny Novgorod, Nizhny Novgorod, Russia, in 1975. He received the Ph.D. and D.Sc. degrees in remote sensing and noninvasive diagnostics from the Radiophysical Research Institute, Nizhny Novgorod, Russia, in 1984 and 1994, respectively.

From 1985 to 1999, he has worked with the Radiophysical Research Institute. From 1999 to present, he is a Leading Scientist with the Institute for Physics of Microstructures RAS, Nizhny Novgorod, Russia. Also, he is a Professor with the Lobachevsky State University of Nizhny Novgorod. He has authored and coauthored more than 300 scientific publications in the area of physical inverse problems, including the book *Inverse problems in physical diagnostics* (New York: Nova Science Inc., 2004). His research interests include electromagnetic and acoustic noninvasive diagnostics and nondestructive testing, images reconstruction and tomography, remote sensing of atmosphere and underlying surface, magnetotelluric and radar subsurface sounding.

Petr K. Gaikovich received the B.S. and M.S. degrees in hydroacoustic tomography from the Lobachevsky State University of Nizhny Novgorod, Nizhny Novgorod, Russia, in 2008 and 2010, respectively.

From 2009 to present, he is with the Institute for Physics of Microstructures RAS, Nizhny Novgorod, Russia, where he works as a Junior Scientist in the region of X-ray multilayer optics. He has authored and coauthored more than 20 scientific publications.

Yelena S. Maksimovitch (M'02–SM'08) received the Ph.D. degree in radiowave polarization-modulation methods of nondestructive testing of the composition materials from the Institute of Applied Physics of the National Academy of Science of Belarus, Minsk, Belarus, in 1999.

In this Institute, she was a Senior Researcher with the Laboratory of Radiowave Methods of the Nondestructive Testing from 1999 to 2004, and from 2004 to present, she is a Leading Researcher with the Laboratory of Radiothomography. She was a Visiting Scientist at the SMARAD/Radio Laboratory (Department of Radio Science and Engineering), Aalto University, Espoo, Finland (1999–2013) for collaborative projects in area of ground penetrating radar, ultra-wideband antennas design. She has authored and coauthored more than 60 scientific publications and 7 certificates of invention and patents. Her research interests include UWB antenna design for near-field applications, methodological support and realization of experiments, development of the microwave methods of nondestructive testing in the building engineering, and biomedical applications.

Dr. Maksimovitch is a member of European Microwave Association (EuMA).

Vitaly A. Badeev was born in Mogilev, Belarus, in 1980. He received the Diploma degree in physics from Belarusian State University, Minsk, Belarus, in 2006.

From 2006 to 2011, he was an Engineer and Junior Researcher with the Laboratory of Microwave Methods for Non-Destructive Testing, Institute of Applied Physics, National Academy of Sciences, Minsk, Belarus. Currently, he is a Researcher with the Laboratory of Radio Tomography, Institute of Applied Physics of the National Academy of Science of Belarus, Minsk, Belarus. He is the coauthor of more than 20 scientific publications and 2 patents. His research interests include electronic engineering, MCU programming (ASM51, C51), and digital signal processing (MATLAB, Signal Processing Toolbox).